

4

THIS FILE COPY

AD-A206 848

LABORATORY OF PLASMA STUDIES

FINAL REPORT

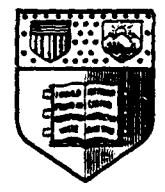
ONR CONTRACT N00014-88-K-2009

INTENSE ION BEAM GENERATION, PLASMA RADIATION SOURCE AND PLASMA OPENING SWITCH RESEARCH

*D.A. Hammer, M.D. Coleman, N. Qi,
P.L. Similon and R.N. Sudan*
Laboratory of Plasma Studies
Cornell University
Ithaca, N.Y. 14853

LPS FR88ONR-1

April 1989



DTIC
ELECTE
S 14 APR 1989 D
E

CORNELL UNIVERSITY
ITHACA, NEW YORK

This document has been approved
for public release and sale; its
distribution is unlimited.

88 14 032

REPORT DOCUMENTATION PAGE

Form Approved
OMB No. 0704-0188

1a. REPORT SECURITY CLASSIFICATION Unclassified			1b. RESTRICTIVE MARKINGS			
2a. SECURITY CLASSIFICATION AUTHORITY			3. DISTRIBUTION / AVAILABILITY OF REPORT			
2b. DECLASSIFICATION / DOWNGRADING SCHEDULE			Unlimited Distribution			
4. PERFORMING ORGANIZATION REPORT NUMBER(S) LPS FR880NR-1			5. MONITORING ORGANIZATION REPORT NUMBER(S)			
6a. NAME OF PERFORMING ORGANIZATION Lab. Plasma Studies Cornell University		6b. OFFICE SYMBOL (if applicable)	7a. NAME OF MONITORING ORGANIZATION SCD-C Martin J. Morris, Resident Representative			
6c. ADDRESS (City, State, and ZIP Code) 369 Upson Hall Ithaca, NY 14853			7b. ADDRESS (City, State, and ZIP Code) 33 Third Ave. - Lower Level New York, New York 10003-6896			
8a. NAME OF FUNDING / SPONSORING ORGANIZATION Naval Research Laboratory		8b. OFFICE SYMBOL (if applicable) Code 4700	9. PROCUREMENT INSTRUMENT IDENTIFICATION NUMBER ONR/N00014-88-K-2009			
8c. ADDRESS (City, State, and ZIP Code) 4555 Overlook Ave. S.W. Washington, DC 20375-5000			10. SOURCE OF FUNDING NUMBERS			
			PROGRAM ELEMENT NO.	PROJECT NO.	TASK NO.	WORK UNIT ACCESSION NO.
11. TITLE (Include Security Classification) Intense Ion Beam Generation, Plasma Radiation Source and Plasma Opening Switch Research						
12. PERSONAL AUTHOR(S) D.A. Hammer, M.D. Coleman, N. Qi, P.L. Similon, R.N. Sudan						
13a. TYPE OF REPORT Final Report		13b. TIME COVERED FROM 1/1/88 TO 12/31/88		14. DATE OF REPORT (Year, Month, Day) 1989, April 3		15. PAGE COUNT 42
16. SUPPLEMENTARY NOTATION						
17. COSATI CODES			18. SUBJECT TERMS (Continue on reverse if necessary and identify by block number)			
FIELD	GROUP	SUB-GROUP	Charged Particle Beams Plasma Opening Switches			
			Intense Ion Beams Plasma Radiation Sources			
			Spectroscopic Diagnostics			
19. ABSTRACT (Continue on reverse if necessary and identify by block number) See Abstract, Page 1						
20. DISTRIBUTION / AVAILABILITY OF ABSTRACT <input checked="" type="checkbox"/> UNCLASSIFIED/UNLIMITED <input type="checkbox"/> SAME AS RPT. <input type="checkbox"/> DTIC USERS			21. ABSTRACT SECURITY CLASSIFICATION Unclassified			
22a. NAME OF RESPONSIBLE INDIVIDUAL David A. Hammer			22b. TELEPHONE (Include Area Code) (607) 255-4127		22c. OFFICE SYMBOL	

TABLE OF CONTENTS

I.	INTRODUCTION	2
	I.A. Summary	2
	I.B. Active Anode Plasma Ion Source for Neptune	2
	I.C. Long Conduction Time Plasma Opening Switch	3
II.	DETERMINATION OF CONDITIONS IN DETAIL IN A PLASMA-PREFILLED ION DIODE BY SPECTROSCOPIC TECHNIQUES	4
	II.A Introduction	4
	II.B The Plasma-Prefilled Ion Diode	5
	II.C LIF Electrostatic Potential Measurement	6
	II.D Discussions and Conclusions	9
	II.E References	
III.	CURRENT PENETRATION AND ION DYNAMICS IN A PLASMA OPENING SWITCH	12
	III.A Introduction	12
	III.B Mathematical Model	12
	III.C Microinstability in the Current Sheath	14
	III.D Solution of Model Equations	15
	III.E Vlasov Approach III.F Two-Dimensional Electron Flow in the Plasma/Cathode Vacuum Gap	20
	III.G Discussion and Conclusions	21
	III.H References	22
	III.I Appendix: Renormalization of Electron and Ion Equations for Microinstabilities	23
IV.	RESULTS OF EXPLORATORY EXPERIMENTS	25
	IV.A Introduction	25
	IV.B Apparatus	26
	IV.C References	36

Accession For	
NTIS GRA&I	<input checked="" type="checkbox"/>
DTIC TAB	<input type="checkbox"/>
Unannounced	<input type="checkbox"/>
Justification	
By _____	
Distribution/	
Availability Codes	
Dist	Avail and/or Special
A-1	

**INTENSE ION BEAM GENERATION,
PLASMA RADIATION SOURCE AND
PLASMA OPENING SWITCH RESEARCH**

D.A. Hammer, M.D. Coleman, N. Qi, P.L. Similon, and R.N. Sudan

Final Report - ONR Contract N00014-88-K-2009

ABSTRACT

This report describes research on intense ion beam diodes, plasma opening switches and dense z-pinch plasma radiators. Laser-induced fluorescence spectroscopy has been used to map the electrostatic potential profile in a plasma-prefilled magnetically insulated ion diode. In a simple planar diode, the measured profile is inconsistent with the electrons being confined in a sheath near the cathode by the magnetic field. Rather, the profile implies the presence of electrons throughout the accelerating gap. A theoretical model of the penetration of current and magnetic field into a plasma, and of the current-driven effective collision frequency has been developed. The snowplow action of the rising magnetic field causes a steep rise in the plasma density at the leading edge. The subsequent multistreaming of the ions caused by ion reflection at the current layer could lead to ion heating through collective effects. The two-dimensional electron flow in the plasma-cathode vacuum gap is also treated. Dense z-pinch plasma radiation source experiments have been initiated on the LION accelerator using gas puff and fine wire loads. The x-pinch was found to be a more effective way to generate soft x-rays than a single wire pinch or a gas puff implosion. Plasma opening switch experiments being initiated,

and plasma anode ion diode development work being terminated are also briefly described.

I. INTRODUCTION

I.A. Summary

During the period 1 January 1988 to 31 December 1988, research was in progress at Cornell University under the support of the Naval Research Laboratory (ONR Contract N00014-88-K-2009) on five research tasks. They were:

1. Design and test an active anode plasma ion source for a 500 kV magnetically insulated diode to be operated on the 3 Ω , 120 ns Neptune Pulsed Power Generator;
2. Carry out spectroscopic investigations of conditions in detail in the high voltage gap of a magnetically insulated ion diode;
3. Initiate experiments on a long conduction time plasma opening switch;
4. Initiate theoretical investigations of plasma opening switches;
5. Initiate experiments and calculations on z-pinch x-ray sources with particular application to photo-pumped or recombination-pumped XUV lasers.

In this report we briefly describe our progress on items 1 and 3 since the first is still in progress, but is no longer supported by NRL, while the third is just beginning. These two are discussed in this introduction. More complete presentations of results on tasks 2, 4, and 5 are presented in Sections II, III, and IV, respectively. Tasks 4 and 5 were also partly supported by the DOE Office of Inertial Fusion.

I.B. Active Anode Plasma Ion Source for Neptune

The motivation for this ion source development task was our successful operation of an active anode plasma ion source on the 150 kV, 1 μ s pulse, 1 Ω LONG-SHOT pulsed power generator under NRL support. The completion of this task

will demonstrate both higher voltage and shorter pulse operation of such a "plasma anode diode." As of the end of the period covered by this final report, the design and construction of the hardware for the plasma anode diode was completed, and vacuum testing was carried out. The diode contains five independent high voltage electrical circuits which must operate correctly to produce the plasma in the desired diode magnetic insulation field configuration, and electrical testing of these circuits had begun. The work is continuing under DOE sponsorship since, by mutual agreement of the Cornell investigators and NRL technical personnel, this work is no longer sponsored by NRL.

I.C. Long Conduction Time Plasma Opening Switch

The success of relatively small and inexpensive pulsed power systems based on inductive energy storage depends on the development of efficient fast opening switches. The long conduction time plasma opening switch (POS) is a good candidate for the last stage opening switch in such a system. A basic understanding of the mechanisms involved in opening are needed to optimize the behavior of these switches. At present they are characterized by longer switching times and more losses than the short conduction time switches.

We have recently begun experiments similar to earlier work at NRL (D.D. Hinselwood et al., Appl. Phys. Lett. 49, 1635 (1986)) to investigate the physics of the operation of long conduction time opening switches. Our emphasis will be on a determination of conditions in detail using spectroscopic diagnostics, although we will also use the usual magnetic probes to monitor current penetration and Faraday cups for plasma flux. The complete system was assembled prior to the end of 1988 and initial experiments were carried out. The results are summarized in the following paragraph. This research is continuing under a new NRL-supported grant.

The POS system is pulsed by a $1.9\mu\text{F}$ Scyllac capacitor charged to 50 kV. It has an inductance of 300 nH (no plasma in the switch, short circuit load) with 10 nH of this downstream of the POS. The plasma for the $10\text{ cm} \times 10\text{ cm}$ planar switch is provided by a Mendel-type carbon plasma gun which is pulsed by a $2.0\mu\text{F}$ capacitor charged to 20 kV. This supplies a plasma with roughly $3 \times 10^{14}\text{ cm}^{-3}$ ion density, predominantly C^{++} , with some C^{+++} , with an electron temperature of 10-15 eV. In a preliminary run with this switch plasma, conduction times up to 400 ns were observed in a short circuit load. An opening time of 130 ns was obtained, delivering 70 kA (out of 106 kA available). An electron beam diode load gave 220 ns conduction time and 190 ns opening time with 70 kA (out of 100 kA available) delivered to the diode with some voltage multiplication. The dynamics of POS operation will be studied in the next experimental series.

II. DETERMINATION OF CONDITIONS IN DETAIL IN A PLASMA-PREFILLED ION DIODE BY SPECTROSCOPIC TECHNIQUES

II.A Introduction

Emission spectroscopy and Laser Induced Fluorescence spectroscopy (LIF) provide potentially valuable techniques for measuring conditions in high voltage gaps non-intrusively. In previous work, the electric field was measured in a magnetically insulated ion diode (MID) using Stark shift emission spectroscopy¹. In this paper, we report measurements of the electrostatic potential profile in a plasma-prefilled MID using LIF. An accelerating gap of 3.5 mm is shown to form in 10^{12} - 10^{14} cm^{-3} argon plasma in a few ns when a 350 kV pulse is applied by a 10Ω pulsed power generator. The observed potential profile for a well insulated gap ($B/B_{crit} = 1.75$, where B is the applied magnetic field and B_{crit} is the minimum field for magnetic insulation² of the actual accelerating gap) is inconsistent with the electrons being confined in a thin sheath by the insulating magnetic field.

II.B The Plasma-Prefilled Ion Diode

Figure II.1 shows an end view of the MID. The anode is connected to the center conductor of a 10Ω pulse line. Argon gas is puffed into the interior of the anode. It is ionized by the electric field induced by the rapidly rising insulating magnetic field of the MID. The magnetic field is generated by current pulsed through the cathode, which acts as a single turn coil. The plasma passes through slots in the anode (oriented vertically in Fig. II.1) and then into the accelerating gap. The slotted area is 6 cm high by 10 cm long. A variable delay adjusts the time of arrival of a 400 kV, 80 ns pulse from the 10Ω pulsed power generator relative to when the plasma is formed. This allows the peak plasma density and the density profile to be varied as part of this experiment. Plasma density in the acceleration gap typically ranges from $\sim 10^{14} \text{ cm}^{-3}$ near the anode to $\sim 10^{12} \text{ cm}^{-3}$ near the cathode at the time the high voltage pulse arrives. Density is determined from the absolute intensity of the 4806\AA Ar^+ line. The spectrometer/photomultiplier system used for this measurement was calibrated by simultaneously measuring the plasma density with a Langmuir probe at one particular location. The plasma temperature was 3.5 eV, as measured from Ar^+ line intensity ratios.

An argon plasma is used for these experiments because of the existence of a metastable state ($3d^4D$) in Ar^+ 16.4 eV above the ground state. Pumping from a ground state or a metastable state is necessary for LIF studies at these plasma temperatures and densities, and pumping from the ground state is difficult due to the large energy separation to the first excited state in most ions.

Figure II.2 shows diode voltage, current, and calculated impedance time histories for a shot with a relatively high density initial plasma-prefill (about 10^{13} cm^{-3} near the cathode). There is an initial period of low diode impedance before the voltage begins to rise. By firing the diode with less plasma in the acceleration gap, significant variation in the impedance characteristics can be obtained, including

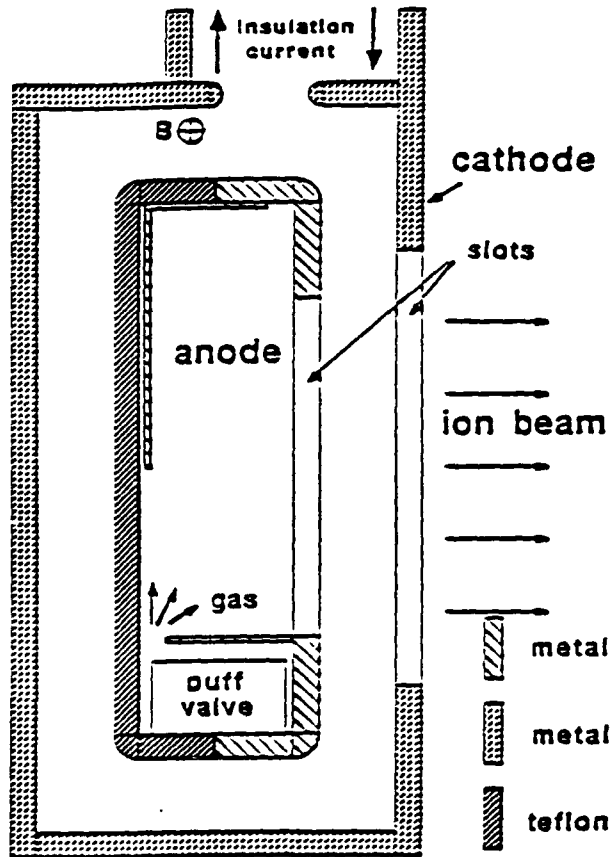


Figure II.1 End view of the plasma-prefilled ion diode.

cases in which the diode impedance is relatively constant throughout the voltage pulse. Typically $30\text{--}60\text{ A/cm}^2\text{ Ar}^+$ beams are extracted as determined from biased Faraday cups.

II.C LIF Electrostatic Potential Measurement

The experimental setup is illustrated in Fig. II.3. A dye laser, tuned near the $4401\text{ \AA}\text{ Ar}^+$ line, is synchronized with the high voltage pulse and directed through slots in the MID cathode (also vertical in Fig. II.1) toward the anode. The laser

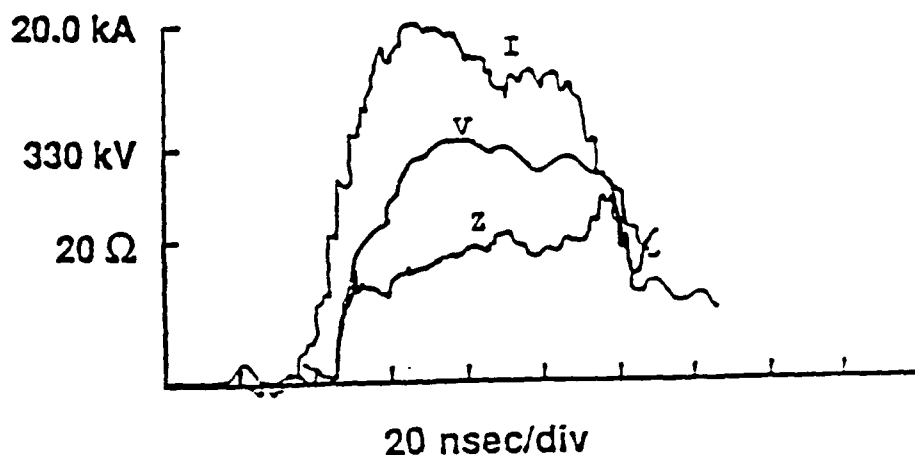


Figure II.2 Time dependence of (from top to bottom) diode current, voltage, and calculated impedance, with scales for each indicated on the ordinate.

light excites electrons from the $3d^4D$ metastable level of the ions to the $4p^4P$ level, from which the ions fluoresce at 4806\AA . The fluorescence emitted perpendicular to the ion beam acceleration direction and along the magnetic field lines is directed into a spectrometer and monitored by a photomultiplier tube. The wavelength for absorption of the laser light by the metastable Ar^+ ions is a function of the distance from the anode, x , since the increasing ion velocity, v , Doppler shifts the wavelength for resonant absorption to values which increase with x . To determine the ion velocity at a particular x , a series of shots is taken tuning the laser to longer and longer wavelength above 4401\AA . The detuning from 4401\AA , $\Delta\lambda$, above which no fluorescence is detected, then determines the velocity at that x :

$$v = (\Delta\lambda/4401)c.$$

The potential drop relative to the anode potential is then given by $\Phi(x) = \frac{1}{2}mv^2$, where m is the mass of an argon atom, and c is the speed of light. A complete $\Phi(x)$ profile is obtained by repeating the procedure with the collection optics for

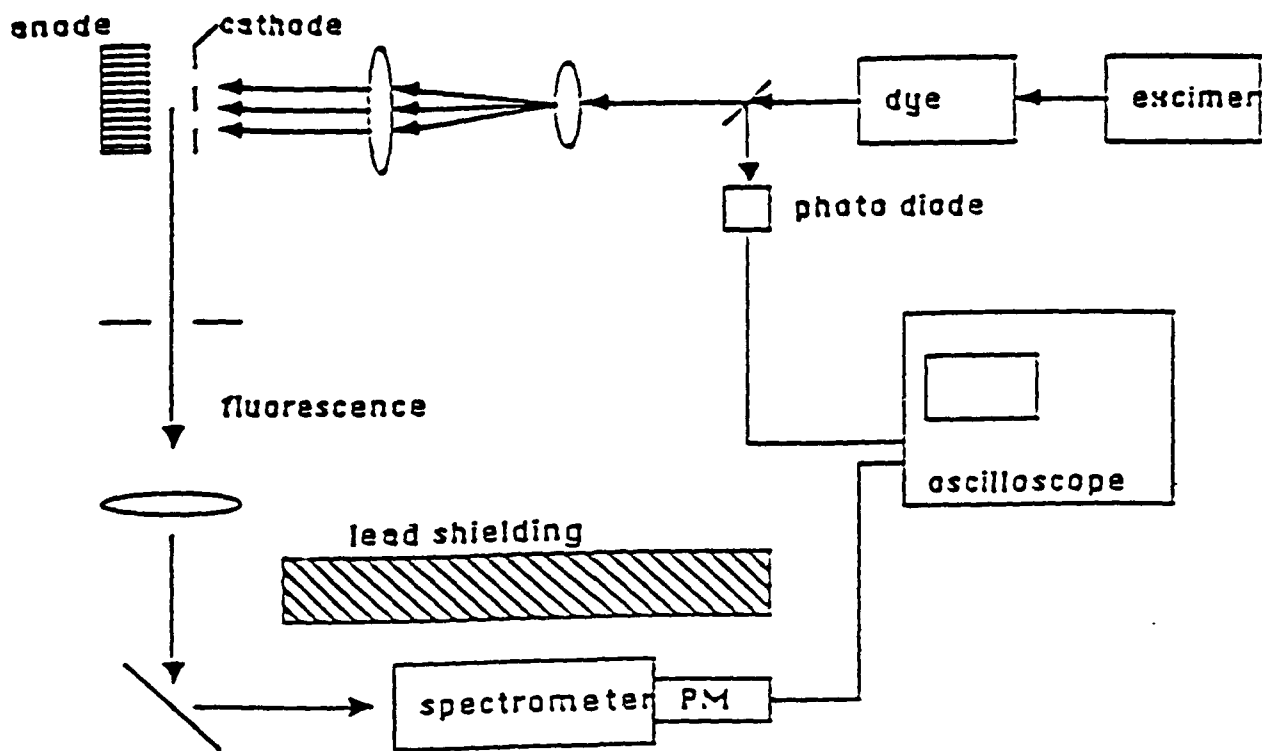


Figure II.3 Schematic diagram of the experimental arrangement

the spectrometer focussed at different values of x .

In the following discussion of results, the laser beam was focussed using a cylindrical lens so that it was about 6 cm wide and about 3 mm high in the acceleration gap. The 15 ns wide (FWHM) pulses contained 12 mJ. The x resolution of the collection optics was 0.5 mm. Figure II.4 shows a typical plot of fluorescence vs. detuning of the laser above the unshifted wavelength for a single x position. Notice that the laser-induced fluorescence drops to zero in $1-1.5\text{\AA}$ around $\Delta\lambda = 13.5\text{\AA}$. This gives $v = 9.2 \times 10^7$ cm/s and $\Phi = 176$ kV for this particular x .

Figure II.5 shows a time history of the potential profile for shots with voltage and current waveforms like those in Fig. II.2, and an insulating B-field of 7 kG. The times 10, 23, 37, and 50 ns are referenced to the time that the current pulse

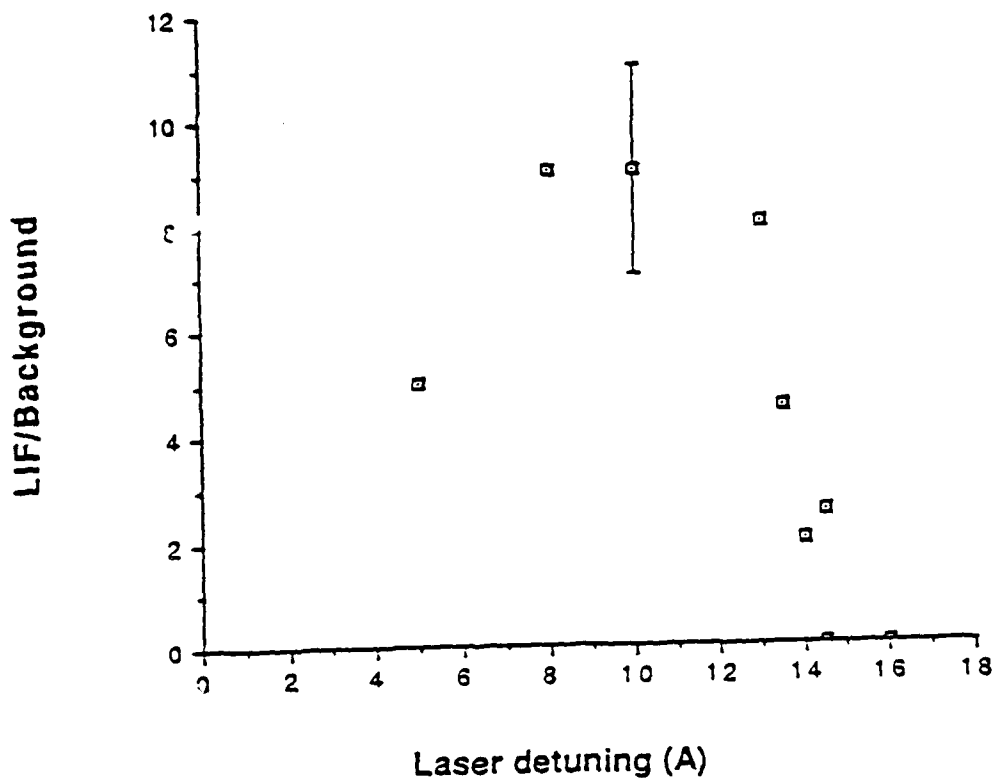


Figure II.4 Typical plot of fluorescence vs. laser detuning.

starts to rise in the diode. (The timing uncertainty is about 2 ns.) Notice that there is a > 8 mm wide region adjacent to the anode which is at anode potential. All of the ion acceleration occurs in a 3.5 mm wide region adjacent to the cathode. The points at the cathode are the inductively corrected voltage obtained from a capacitive probe on the end of the pulseline. Such voltage measurements are always consistent with the ion kinetic energies measured by the LIF technique after the ions have been extracted from the diode within 10%.

II.D Discussions and Conclusions

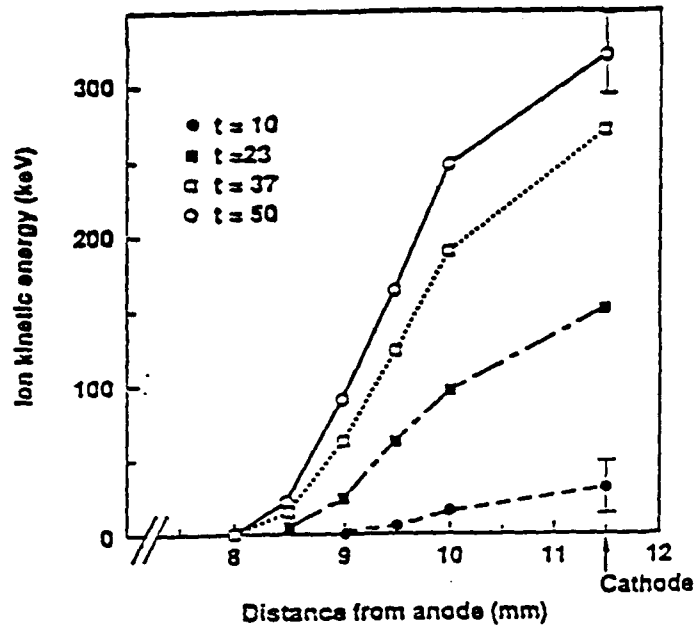


Figure II.5 Time dependence of ion kinetic energy (which equals the potential drop from the anode) as a function of distance from the anode. At $t = 50$ ns, $B/B_{crit} = 1.1$. The metal anode is at $x = 0$.

The data shown in Fig. II.5 was selected for presentation because the density was high enough that the opening up of the acceleration gap was visible. The corresponding voltage waveform is shown in Fig. II.2. Thus, the impedance history of the gap during the first 15 ns is similar to that observed for a plasma opening switch.

Potential profiles have also been obtained for a plasma-prefill about a factor of three lower density than was the case when the profiles in Fig. II.5 were obtained. In that case, the diode voltage and current rise together. Finally, we have also investigated diode configurations in which electron emitting vanes have been added to the cathode. In cases in which the effective diode gap (the gap between the cathode and the largest x at anode potential) is well insulated (e.g. - $B/B_{crit} = 1.75$), the potential profile clearly does not correspond well to models involving a well confined electron sheath.³ Instead, the profile corresponds nicely with the simple assumption of uniform electron density in the accelerating gap, in qualitative

agreement with the electric field measurements made in a surface flashover MID using emission spectroscopy by Maron et al.¹

This LIF potential measuring technique could possibly be utilized in other, higher power ion diodes which cannot use argon gas as the anode plasma source, by seeding the plasma with desirable impurities (e.g.- calcium, in which pumping from the ground state of the ion is possible). Also, this technique could possibly be put to great use as a non-intrusive method to measure voltages (as small as 2 kV) as a function of all spatial directions in plasma opening switches.

II.E References

1. Y. Maron, M.D. Coleman, D.A. Hammer, and H.S. Peng, Phys. Rev. A **36**, 2818 (1987).
2. R. N. Sudan and R. V. Lovelace, Phys. Rev. Lett. **31**, 1174 (1973).
3. T.M. Antonsen, Jr., and E. Ott, Phys. Fluids **19**, 52 (1976).

III. CURRENT PENETRATION AND ION DYNAMICS IN A PLASMA OPENING SWITCH

III.A Introduction

Progress in the physics and technology of plasma opening switches (POS) for pulsed power systems in the terawatt, less than 100 nanosecond, range has been reported recently in the Dec. 1987 issue of Plasma Science.¹ There is, however, considerable controversy over the physical mechanisms underlying the operation of this switch. In the main there are two interpretations of switch operation. The NRL group² maintains that in the later stages the electrons are magnetically insulated by their self-magnetic field and are unable to cross the gap between the cathode and the plasma. The conduction current is therefore provided by the plasma ions and because this is greatly in excess of the ion thermal flux, results in the erosion of the plasma surface facing the cathode thereby increasing the A-K gap and eventually to current interruption. The alternative picture³ argues that the magnetic $\mathbf{j} \times \mathbf{B}$ forces must play a strong role in the current interruption process.

In this paper we address the issues of (i) current penetration into a plasma from a high power travelling electromagnetic pulse incident on the surface of plasma created in a transmission line, (ii) the ion dynamics, and (iii) the two-dimensional electron flow in the plasma/cathode vacuum gap. A proper understanding of these problems is an absolute requisite for any POS model.

III.B Mathematical Model

We consider a one-dimensional representation of the plasma, deferring the consideration of cathode and anode sheaths to Section VI. Plasma quasineutrality is assumed i.e., $n_e = n_i = n$; the ions are taken to be singly ionized without much loss in generality. In the two-fluid approximation the equations governing plasma

behaviour are given by:

$$\frac{\partial n}{\partial t} + \frac{\partial}{\partial x} (nv) = 0, \quad (1)$$

$$\frac{\partial}{\partial t} (\rho v) + \frac{\partial}{\partial x} \left(\rho v^2 + \frac{B^2}{8\pi} \right) = 0, \quad (2)$$

$$\frac{\partial}{\partial t} p + v \frac{\partial}{\partial x} p = -m\nu w, \quad (3)$$

$$\frac{\partial B}{\partial x} = \frac{\partial^2 A}{\partial x^2} = 4\pi n e w / c, \quad (4)$$

Here $\rho = nM$ is the plasma mass density, $v_e = v_i = v$ is the x-component of the ion and electron velocities, w is the electron y-velocity, $p = m\gamma w - eA/c$ is the electron y-canonical momentum, $\gamma = (1 - (v^2 + w^2)/c^2)^{-\frac{1}{2}}$, $\mathbf{B} = B \hat{z}$ and the vector potential $\mathbf{A} = A \hat{y}$. The momentum transfer between electrons and ions is determined by the collision frequency ν which signifies both Coulomb collisions and collective effects due to microinstabilities. Equation (3) expresses the conservation of the electron y-canonical momentum if the collisions are infrequent. The pressure is neglected because the initial plasma β in the current sheath is small.

In the collisionless limit $\partial p / \partial t \gg m\nu w$, Eqns. (3) and (4) may be combined to give

$$\frac{\partial^2 A}{\partial x^2} = \frac{4\pi n e^2 A}{m c^2} \left[1 + \left(\frac{eA}{m c^2} \right)^2 \right]^{-\frac{1}{2}}. \quad (5)$$

In the non-relativistic limit $eA \ll mc^2$ this equation determines the current sheath thickness Δ to be of order $\lambda_E = c/\omega_e$, $\omega_e^2 = 4\pi n_0 e^2/m$. In the ultra-relativistic limit $eA \gg mc^2$ and $B = B_0(x=0) - 4\pi n_0 e x$. This solution is limited to $t < \Delta/c_A$, [$c_A = B_0/(4\pi\rho_0)^{\frac{1}{2}}$ is the Alfvén velocity], during which the density n does not change significantly from the initial value n_0 . Note that in the ultrarelativistic limit $\Delta = B_0/4\pi n_0 e$.

In almost all instances of pulsed power POS applications the electron drift velocity in the current sheath far exceeds the acoustic speed $c_s = (T/M)^{\frac{1}{2}}$ and perhaps

even approaches or exceeds $(T/m)^{1/2}$ the electron thermal speed. The microinstabilities excited by the current lead to an enhanced rate of momentum transfer from the electrons to the ions or to the emitted waves.⁴ This increase in the effective collision frequency ν_* may cause the collisional term in Eqn. (3) to dominate the electron mechanical inertia. If this limit obtains Eqns. (3) and (4) may be combined to give

$$\frac{\partial B}{\partial t} + \frac{\partial}{\partial x} (vB) = \frac{\partial}{\partial x} \eta \frac{\partial B}{\partial x}, \quad (6)$$

where $\eta = (c^2 m \nu_* / 4\pi n e^2)$. Thus the collisionless limit is defined by Eqns. (1), (2) and (5) and the collisional limit by Eqns. (1), (2) and (6).

III.C Microinstability in the Current Sheath

A recent calculation by Kulsrud et al.⁵ explores the consequences of ion acoustic waves driven unstable by the electron drift. They show that wave emission by the electrons leads to a drag force on the electrons in the y-direction which is equivalent to an effective collision frequency

$$\nu_* = (\pi/2)^{1/2} (k_y^2/k_{||}) (T/m)^{1/2} (e \tilde{\phi}/T)^2, \quad (7)$$

where the spectrum has a mean wave-vector $\mathbf{k} = (0, k_y, k_{||})$ and $\tilde{\phi}$ is the amplitude of the electric potential fluctuations.

If, as suggested by Kulsrud et al.⁵, we set $k_y \lambda_D \sim 1$, (λ_D is the Debye length) $k_{||} v_e \sim k_y w$, (v_e and w are the electron thermal and drift velocities), and $e \tilde{\phi}/T \sim 1$, one obtains $\nu_* \sim \omega_e (v_e/w)$, where ω_e is the electron plasma frequency. At the high saturation amplitude chosen $e \tilde{\phi}/T \sim 1$ the nonlinear distortion of the electron orbits⁶ by the emitted wave fields, omitted in the earlier analysis,⁵ must be taken into account. In the Appendix we employ the nonlinear drift-kinetic equation for the electrons and compute the renormalization of the wave growth rate due to stochastic diffusion of electron trajectories in the emitted fields. We also consider

the nonlinear exchange of momentum between the waves and the ions, which is expressed in terms of an anomalous "eddy" viscosity. At the saturation intensity, the ion damping balances the electron excitation, and therefore limits the fluctuation amplitude to

$$e\bar{\phi}/T \sim (\Omega_e/kv_e)^{1/3}(w/v_e)^{1/3} \ll O(1); \quad 1 > kv_e/\Omega_e \gg w/v_e. \quad (8a)$$

The momentum transfer rate from electrons to waves is reduced due to nonlinear scattering with respect to the linear estimate. Altogether, it is found that the effective collision frequency is a factor

$$\frac{1}{3}(\Omega_e/kv_e)^{4/3}(w/v_e)^{4/3} \ll 1 \quad (8b)$$

smaller than Kulsrud *et al.*'s⁵ estimate.

III.D Solution of Model Equations

Equations (1), (2), (5), and (6) may be expressed in Lagrangian variables through a coordinate transformation $(x, t) \iff (\xi(x, t), \tau)$ such that $\xi = x$ at $t = 0$ and,

$$\frac{d\xi}{dt} = \frac{\partial \xi}{\partial t} + v \frac{\partial \xi}{\partial x} = 0, \quad (9)$$

$$\tau = t. \quad (10)$$

Thus, because of density conservation,

$$\partial \xi / \partial x = n(\xi, \tau) / n_0(\xi), \quad (11)$$

where $n_0(\xi)$ is the initial density profile at $\tau = 0$. In the new coordinates Eqns. (1) and (2) become

$$\frac{\partial}{\partial \tau} (n_0/n) - \frac{\partial v}{\partial \xi} = 0, \quad (12)$$

$$\frac{\partial v}{\partial \tau} + \frac{1}{n_0} \frac{\partial}{\partial \xi} \frac{B^2}{8\pi M} = 0. \quad (13)$$

Combining (12) and (13) we get

$$\frac{\partial^2}{\partial \tau^2} \left(\frac{1}{n} \right) + \frac{1}{n_0} \frac{\partial}{\partial \xi} \frac{1}{n_0} \frac{\partial}{\partial \xi} \frac{B^2}{8\pi M} = 0. \quad (14)$$

For the collisionless case Eqn. (5) transforms to

$$\frac{\partial B}{\partial \xi} = \frac{4\pi n_0(\xi) e^2}{mc^2} A \left[1 + \left(\frac{eA}{mc^2} \right)^2 \right]^{-\frac{1}{2}}. \quad (15)$$

In the ultrarelativistic case the exact solution of (15) is

$$B(\xi) = B_0 - 4\pi e \int^\xi n_0 d\xi \quad (16)$$

even when the plasma dynamics is taken into account. For the collisional case, Eqn. (6) transforms to

$$\frac{\partial}{\partial \tau} (n_0 B/n) = \frac{\partial}{\partial \xi} \eta_0 \frac{\partial B}{\partial \xi}, \quad (17)$$

where $\eta_0 = c^2 m \nu_* / 4\pi n_0 e^2$ and B at $\xi = 0$ is equal to $B_0(\tau)$, a given function determined by the imposed current pulse. In terms of the vector potential A , Eqn. (17) may be rewritten as

$$\frac{\partial A}{\partial \tau} = \eta_0 \frac{\partial}{\partial \xi} \left(\frac{n}{n_0} \frac{\partial A}{\partial \xi} \right). \quad (18)$$

Ultra-relativistic Collisionless Case

We treat this case because of its simplicity, its relevance for very high currents and also because it reveals a very important feature of this problem. Substituting Eqn. (16) in Eqn. (14) yields,

$$\frac{\partial^2}{\partial \tau^2} \left(\frac{1}{n} \right) + \frac{4\pi e^2}{M} = 0, \quad (19a)$$

thus

$$n(\xi, \tau) = n_0(\xi) \left[1 - \frac{1}{2} \omega_i^2 \tau^2 \right]^{-1}, \quad (19b)$$

for $\xi < \xi_c$, where $B_0 = 4\pi e \int_0^{\xi_c} n_0 d\xi$ and $\omega_i^2 = 4\pi n_0(\xi) e^2 / M$. We notice immediately that a singularity arises in the density at $\tau_1 = \sqrt{2}/\omega_i$. This singularity signals the breakdown of the fluid description and this occurs in a time much less than a plasma ion period! The flow velocity is given by

$$v(\xi, \tau) = \left[eB_0/M - (4\pi e^2/M) \int_0^{\xi} d\xi n_0 \right] \tau. \quad (20)$$

Collisional Case

The singularity in density arises also in the collisional case. From Eqn. (17) with $B(\xi = 0, \tau)$ determined by the external current as a monotonically increasing function of τ , it is apparent that $B(\xi, \tau)$ will be a monotonically decreasing function of ξ for fixed τ , because of the diffusive nature of this equation. Consequently the second term of Eqn. (14) will be positive definite. Thus

$$\frac{\partial^2}{\partial \tau^2} (1/n) = - \frac{1}{n_0} \frac{\partial}{\partial \xi} \frac{1}{n_0} \frac{\partial}{\partial \xi} \frac{B^2}{8\pi M} \equiv -K(\xi, \tau)$$

and

$$n(\xi, \tau) = n_0(\xi) \left[1 - \int_0^{\tau} d\tau' \int_0^{\tau'} d\tau'' K(\xi, \tau'') \right]^{-1}. \quad (21)$$

From dimensional consideration of Eqns. (14) and (17) the approximate order of time needed for the singularity to develop is $\tau_2 \approx 2\nu_*/\Omega_e\Omega_i$, where Ω_e and Ω_i are the electron and ion cyclotron frequencies in B_0 . In the non-relativistic collisionless case $\tau_1 \approx 2/\sqrt{\Omega_e\Omega_i}$. Thus, if $\tau_2 < \tau_1$, i.e.,

$$\nu_*/2\sqrt{\Omega_e\Omega_i} < 1, \quad (22)$$

the situation is treated as collisionless and collisional if the above inequality is violated.

The physical implication of the singularity in density is that the snowplowing action of the magnetic field results in the generation of a reflected stream of ions

from the current layer because of the electrostatic potential in the current layer given by

$$\frac{\partial \varphi}{\partial \xi} = \frac{w}{c} \frac{\partial A}{\partial \xi} = \frac{1}{8\pi n_0 e} \frac{\partial}{\partial \xi} B^2. \quad (23)$$

An approximate expression for the potential drop in x is $e\varphi_0 \approx B_0^2/8\pi n_0 e$ (in the ultrarelativistic limit $\varphi \approx A$).

III.E Vlasov Approach

The effect of thermal spread in the ion dynamics is obtained through the Vlasov equation for the ion distribution $f(v_x, v_y, x, t)$ which for our problem becomes

$$\frac{\partial f}{\partial t} + v_x \frac{\partial f}{\partial x} + \frac{e}{M} \left(-\frac{\partial \varphi}{\partial x} + \frac{v_y}{c} \frac{\partial A}{\partial x} \right) \frac{\partial f}{\partial v_x} - \frac{e}{Mc} \left(\frac{\partial A}{\partial t} + v_x \frac{\partial A}{\partial x} \right) \frac{\partial f}{\partial v_y} = 0. \quad (24)$$

We may neglect $(v_y/c) \partial A/\partial x$ as compared to $-\partial \varphi/\partial x$, (see Eqn. (23)) and employ the transformation to the Lagrangian coordinate ξ as in Eqn. (9). Expressing f also as a function of the ion canonical y -momentum $P = Mv_y + eA/c$, Eqn. (24) reduces to

$$\frac{\partial f}{\partial \tau} + (v_x - v) \frac{\partial f}{\partial \xi} - \frac{1}{n_0 M} \frac{\partial}{\partial \xi} \left(\frac{B^2}{8\pi} \right) \frac{\partial f}{\partial v_x} = 0. \quad (25)$$

The characteristics of this equation are determined by

$$n_0 d\xi/n [v_x - v(\xi, \tau)] = dv_x / (\partial/n_0 \partial \xi) B^2 / 8\pi M = d\tau,$$

from which we obtain

$$\bar{\xi} + \xi^2 \frac{\partial}{\partial \xi} \ln(n_0/n) + 2\xi \frac{\partial}{\partial \tau} \ln(n_0/n) = -\frac{n}{n_0} \frac{\partial v}{\partial \tau} + \frac{n}{(n_0)^2} \frac{\partial}{\partial \xi} (B^2/8\pi M). \quad (26)$$

In the hydrodynamic limit with no thermal spread, the ions do not move with respect to the background plasma, $\dot{\xi} = 0 = \bar{\xi}$, and we recover Eqn. (13). The trajectory of a test particle which has a thermal velocity δv_x in excess of the hydrodynamic velocity $v(\xi, \tau)$ at $\tau = 0$ is obtained from Eqn. (26) to be

$$\bar{\xi} = \delta v_x (n/n_0) \exp - \int_0^\tau d\tau \frac{\partial}{\partial \tau} \ln(n_0/n), \quad (27)$$

where n/n_0 is a function of ξ, τ obtained from the hydrodynamic equations. In the ultrarelativistic limit, (n/n_0) is not explicitly dependent on ξ , Eqn. (19b) provided $0 < \xi < \xi_c$, and Eqn. (27) can be readily integrated to give $\dot{\xi} = \delta v_x (\frac{n}{n_0})^2$. Thus the ion temperature $\sim \langle (\dot{\xi} n_0/n)^2 \rangle$ increases dramatically.

After $\tau = \tau_1$ or τ_2 the time taken for a singularity to develop in the density, multistreaming takes place and our Lagrangian transformation which depends on a one to one correspondence between x and ξ is no longer valid. The effect of a thermal spread in the ions is to reduce the magnitude of the density increase because all the particles will not arrive at the same time at the same point.

The physical consequences of ion reflection at the current layer after $\tau \equiv \tau_1$ or τ_2 , is the development of ion viscosity between the incoming and reflected ions as a result of micro-instabilities such as the lower-hybrid. However, these instabilities will only occur in the current layer where a finite magnetic field exists. If the ion slowing down length (as a result of ion viscosity) is greater than the current layer width Δ , the reflected ions will proceed in ballistic orbits in the magnetic field-free region of the plasma.

Because of the complications introduced by multistreaming after $\tau = \tau_1$ or τ_2 , analytical solutions are abandoned in favor of a numerical solution. The basic equations for a simple one-dimensional hybrid code under development in which the electrons are treated as a massless fluid and the ions as discrete particles, are as follows:

$$\ddot{x}_j = \frac{e}{Mc} \left\{ \left(u_y + \frac{c}{4\pi ne} \frac{\partial^2 A}{\partial x^2} \right) \frac{\partial A}{\partial x} + \dot{y}_j \frac{\partial A}{\partial x} \right\}, \quad (28)$$

$$\ddot{y}_j = -\frac{e}{Mc} \dot{A} + \frac{e}{Mc} \left(\frac{\partial A}{\partial t} + u_x \frac{\partial A}{\partial x} \right) = -\frac{e}{Mc} (\dot{x}_j - u_x) \frac{\partial A}{\partial x}, \quad (29)$$

$$\frac{\partial A}{\partial t} + u_x \frac{\partial A}{\partial x} = \frac{mc^2 \nu}{4\pi ne^2} \frac{\partial^2 A}{\partial x^2} \quad (30)$$

where the mean velocities of particle ions

$$\begin{pmatrix} u_x \\ u_y \end{pmatrix} = \frac{1}{N} \sum_{j=1}^N \begin{pmatrix} \dot{x}_j \\ \dot{y}_j \end{pmatrix}$$

at the location x and n is the mean ion density.

III.F Two-Dimensional Electron Flow in the Plasma/Cathode Vacuum Gap

We show below that the current between the cathode and the plasma in the vacuum gap can be carried by the electrons even when strongly magnetized in a two-dimensional equilibrium flow. We have extended some earlier calculations of Sudan⁷ in which the electrons are treated as a fluid obeying the following equations:

$$\nabla^2 \varphi = 4\pi ne, \quad (31)$$

$$\mathbf{j} = \frac{c}{4\pi} \nabla \times \mathbf{B} = \frac{c}{4\pi} \nabla B \times \hat{z} = -nev, \quad (32)$$

$$\mathbf{v} \cdot \nabla \mathbf{v} = (e/m) (\nabla \varphi - \mathbf{v} \times \mathbf{B}/c) - \nabla U, \quad (33)$$

where U is the electron enthalpy per unit mass and the electron fluid is assumed to be isentropic. We take $\partial/\partial z = 0$ and $\mathbf{B} = B(x, y)\hat{z}$. From Eqns. (33) and (32) it is easy to derive

$$\mathbf{v} = (\hat{z} \times \nabla \psi) / (\Omega - \omega), \quad (34)$$

$$\mathbf{j} = (\nabla \psi \times \hat{z}) ne / (\Omega - \omega) = (c/4\pi) \nabla B \times \hat{z}, \quad (35)$$

with $\psi \equiv e\varphi/M - v^2/2 - U$, $\Omega = eB/mc$ and $\omega = \hat{z} \cdot \nabla \times \mathbf{v} = \nabla \cdot \mathbf{v} \times \hat{z}$ is the electron vorticity. We now specialize to a class of solutions such that

$$n(x, y)/B(x, y) = n_0/B_0 = \text{constant}, \quad (36)$$

$$\omega(x, y)/\Omega(x, y) = \omega_0/\Omega_0 = \text{constant}. \quad (37)$$

From (35), (36), and (37) we conclude that

$$B = 4\pi m(n_0/B_0) (1 - \omega_0/\Omega_0)^{-1} \psi, \quad (38)$$

$$\frac{\partial^2 b}{\partial x^2} + \frac{\partial^2 b}{\partial y^2} = e^{-b}, \quad (39)$$

$$\frac{\partial^2 \Phi}{\partial x^2} + \frac{\partial^2 \Phi}{\partial y^2} = \left| \frac{\Omega_0}{\omega_0} \right| e^{-b}, \quad (40)$$

where $e^{-b} = B/B_0$, $\Phi = e\varphi/mc^2$, $\Omega_0\omega_0 < 0$, and the coordinates x and y have been normalized by the length $l = [B_0/(4\pi n_0 m)^{1/2}]/|\omega_0\Omega_0|^{1/2}$. Equation (39) is the Liouville equation with the solution⁸

$$e^{-b} = 8[(\partial g^2/\partial x)^2 + (\partial g^2/\partial y)^2]/(1 + g^2 + h^2)^2, \quad (41)$$

$f(\zeta) = f(x + iy) = g(x, y) + ih(x, y)$ is an arbitrary single valued analytic function chosen to fit the boundary conditions. Once b is solved the electrostatic potential may be obtained from Eqn. (40). The characteristic width of the current layer in the vacuum gap is

$$l = [B_0/(4\pi n_0 m)^{1/2}]/(\omega_0\Omega_0)^{1/2} = \alpha^{-1/2}(c/\omega_e) \equiv \lambda_E/\alpha^{1/2}$$

where $\alpha = |\omega_0/\Omega_0| < 1$. Equation (39) is solved by demanding $B = B_0$ along a profile which connects the electron sheath surface of the incoming electromagnetic pulse to the plasma surface, and $B = B_a(x)$ along the plasma surface; $B(x) \rightarrow 0$ as $x \gg l$.

III.G Discussion and Conclusions

Our principal conclusions are as follows: (1) The renormalized estimate of the electron collision frequency is much less than ω_e and the electron heating rate is correspondingly reduced. (2) The snowplow action of the magnetic field increases the plasma density rapidly in a time $\tau_1 \sim 2/\sqrt{\Omega_e\Omega_i}$ or $\tau_2 \sim 2\nu_e/\Omega_e\Omega_i$; causing

rapid ion heating. The counterstreaming ions lead to ion viscosity and to further ion heating due to collective effects. (3) The snowplow velocity is approximately $B_0/\sqrt{8\pi n_0 M}$. Near the cathode and anode the density n_0 is expected to be less than in the bulk plasma. Thus the snowplow action is more rapid near the electrodes and creates vacuum gaps between the plasma and the electrodes. Subsequently snowplow action pushes the plasma away from the electrodes, as well as reducing the x-dimension. (4) Electrons can cross the vacuum gap in a strong magnetic field by virtue of a two-dimensional equilibrium. When the electrode gaps become very large as a result of snowplow action the boundary conditions for even a two-dimensional flow may not be satisfied causing current interruption. (5) Plasma surfaces may be rippled by the Rayleigh-Taylor instability with a typical wavelength \sim current sheath thickness.

III.H References

1. Special Issue on Fast Opening Vacuum Switches, IEEE Trans. Plasma Science, vol. PS-15, Dec. 1987.
2. P. F. Ottinger, S. A. Goldstein and R. A. Meger, J. Appl. Phys. 56, 774, 1984.
3. C. W. Mendel, private communication.
4. See for example: A.A. Galeev and R. Z. Sagdeev, Current Instabilities and Anomalous Resistivity in a Plasma, Chap. 6.1, Basic Plasma Physics, Handbook of Plasma Physics, Vol. II, Ed. A. A. Galeev and R. N. Sudan, North Holland Publishing Co., New York, N.Y. (1984).
5. R. M. Kulsrud, P. F. Ottinger and J. M. Grossmann, to appear in Phys. Fluids (1988).
6. T. H. Dupree, Phys. Fluids, 9, 1773 (1966).
7. R. N. Sudan, Proc. 4th Int. Conf. on High Power Electron and Ion Beams, Ed. H. J. Doucet and J. M. Buzzi, Palaiseau, France (1981), Vol. I, p. 389.
8. W. F. Ames, Nonlinear Partial Differential Equations in Engineering, Academic Press, New York (1967).

III.I Appendix: Renormalization of Electron and Ion Equations for Microinstabilities

We examine nonlinear effects on the effective electron collision frequency ν_* due to ion acoustic instability computed by Kulsrud et al.⁵ The stochastic electron $\mathbf{E} \times \mathbf{B}$ motion decorrelates the electrons from the waves, thereby reducing the growth rate. The ions are also subject to random motion and the resulting eddy viscosity absorbs wave momentum and saturates the acoustic wave intensity $(e\tilde{\phi}/T)^2$ to much less than unity. The reduced rate of momentum transfer from electrons to waves results in a lower ν_* than the linear estimate of Kulsrud et. al.⁵

The electrons are governed by the drift-kinetic equation ($|\omega - k_{\parallel}v_{\parallel} - k_y w| \ll \Omega_e, k_{\perp}v_e \ll \Omega_e$)

$$\partial f / \partial t + \mathbf{v}_E \cdot \nabla f + v_{\parallel} \nabla_{\parallel} f - (e/m)\mathbf{E}_{\parallel} \partial f / \partial v_{\parallel} = 0 \quad (A1)$$

and the ions by the fluid equations neglecting pressure. Quasineutrality and the electrostatic approximation apply. The renormalized drift equation for the fluctuations is

$$-i(\omega - k_{\parallel}v_{\parallel} - k_y w - k_x u_a)\tilde{f} + i(e/m)k_{\parallel}(\partial f_0 / \partial v_{\parallel})\tilde{\phi} + k_x^2 D_s(\tilde{f} - f_0 e\tilde{\phi}/T) + \frac{\partial}{\partial v_{\parallel}} D_v \frac{\partial}{\partial v_{\parallel}} \tilde{f} = 0 \quad (A2)$$

where $k_{\perp}^2 = k_x^2 + k_y^2 \gg k_{\parallel}^2$, w and u_a are the drifts due to the electrostatic field given by Eqn. (23) and by the drag force on electrons by the emitted acoustic waves respectively, $D_s \sim \langle |\delta \mathbf{v}_E|^2 \tau_e \rangle$ is the diffusivity of the nonadiabatic electron fluctuations due to random $\mathbf{E} \times \mathbf{B}$ motion, and $D_v \sim \langle |e\mathbf{E}_{\parallel}/m|^2 \tau_e \rangle$ is the diffusivity in v_{\parallel} -space due to random acceleration by \mathbf{E}_{\parallel} . Here τ_e^{-1} is the largest of the decorrelation rates due to (i) electron transit frequency in the wavepacket $\tau_e^{-1} \sim \Delta k_y w$, (ii) nonlinear decorrelation frequencies $k^2 D_s$ and D_v/v_e^2 . For a high level of fluctuations, the perpendicular diffusion is dominant. Thus $\tau_e^{-1} \sim$

$k^2 D_e \sim (k^2 v_e^2 / \Omega_e) \langle |e\tilde{\phi}/T| \rangle > \Delta k_y w$. It turns out that this demands $kv_e/\Omega_e \gg w/v_e$. For these large decorrelation rates Eqn. (A2) may be approximated by $\tilde{f} \approx \left(1 + i \frac{\omega - k_y w}{k^2 D_e}\right) f_0 \frac{e\tilde{\phi}}{T}$. The electrons behave like a fluid and integrating over v_{\parallel} we get

$$\frac{\tilde{n}}{n_0} \approx \left(1 + i \frac{\omega - k_y w}{k^2 D_e}\right) \frac{e\tilde{\phi}}{T}. \quad (\text{A3})$$

The ions are unmagnetized since $\omega \gg \Omega_i$ and in the renormalized ion equations, the nonlinear term $\mathbf{u} \cdot \nabla \mathbf{u}$ is replaced by the eddy viscosity $-D_i \nabla^2 \mathbf{u}$, where $D_i \sim \frac{\langle |u|^2 \rangle}{(\Delta k) c_s}$. The momentum equation gives $\mathbf{u} = c_s^2 \frac{\mathbf{k}}{\omega + ik^2 D_i} \frac{e\tilde{\phi}}{T}$ and from the continuity equation we obtain

$$\frac{\tilde{n}}{n_0} \approx c_s^2 \frac{k^2}{\omega(\omega + ik^2 D_i)} \frac{e\tilde{\phi}}{T} \quad (\text{A4})$$

where $D_i \sim \frac{c_s^2}{\langle \omega \rangle} \langle | \frac{e\tilde{\phi}}{T} |^2 \rangle$. Quasineutrality then furnishes the dispersion relation

$$\frac{\omega^2}{k^2 c_s^2} = \left(1 + i \frac{k^2 D_i}{\omega}\right)^{-1} \left(1 + i \frac{\omega - k_y w}{k^2 D_e}\right)^{-1} \quad (\text{A5})$$

from which we obtain the frequency $\omega_r \approx kc_s$ and the renormalized growth rate $\bar{\gamma}$

$$\bar{\gamma}/\omega_r \approx -\frac{k^2 D_i}{2\omega_r} + \frac{k_y w - \omega_r}{2k^2 D_e} \quad (\text{A6}).$$

For comparison, the linear growth rate γ derived by Kulsrud et. al.⁵ (but valid only for $\omega_e \ll \Omega_e$) is $\gamma/kc_s \approx 1.5 \frac{k_y w - \omega_r}{|k_{\parallel}| v_e}$. Not only does the turbulence reduce the electron energy input, but it also damps the waves by allowing transfer of momentum from waves to ions. As a first estimate of saturation level, set $\bar{\gamma} = 0$ to obtain $\langle | \frac{e\tilde{\phi}}{T} | \rangle \sim (w/v_e)^{\frac{1}{3}} (\Omega_e/kv_e)^{\frac{1}{3}} \ll 1$. The momentum transfer rate from electrons to waves is proportional to the second term on the RHS of (A6). Hence,

$$\frac{\nu_e(\text{renorm.})}{\nu_e(\text{Kulsrud et. al.})} = \frac{1}{3} (w/v_e)^{\frac{4}{3}} (\Omega_e/kv_e)^{\frac{4}{3}} \ll 1 \text{ since as noted above that}$$

$$1 > kv_e/\Omega_e \gg w/v_e.$$

IV. RESULTS OF EXPLORATORY EXPERIMENTS

IV.A Introduction

In order to determine the feasibility of using LION for gas puff implosions and with fine wire loads, and to test the relative soft x-ray yield of different z-pinch load configurations with a constant input power pulse, two exploratory series of experiments have been performed. Approximately 100 test pulses were carried out all told. Most of them were gas puff implosions, a few of which were carried out using a stabilizing magnetic field. About 30 shots used carbon and/or aluminum fiber loads to form the z-pinch, including single fiber, x-pinch and "double-cross" configurations. There were also some short circuit calibration pulses and one "open circuit" test.

The "project-oriented" goal of the first set of the experiments was to learn to set up and carry out well-diagnosed z-pinch experiments with a full power pulse on LION. We believe we achieved that project-oriented goal: we obtained useful data on 45 of 70 pulses with a full set of diagnostics, and many of those pulses were carried out at or above 90% of full generator power. About 40 pulses utilized acetylene gas (C_2H_2) in the puff valve, while the remaining 20 were done with carbon monoxide (CO). About 10 tests were performed with very fine ($6\ \mu m$ mean diameter) carbon filaments. Included in the diagnostic package in the first experimental series was a "McDonald" soft x-ray spectrograph which we borrowed from Sandia National Laboratories, Albuquerque (SNLA).

In the second (25 pulse) series of experiments, the McDonald spectrograph was not available. Therefore, the emphasis was on obtaining x-ray yield information for different z-pinch configurations driven by the same input power pulse.

In the following paragraphs, we briefly describe the apparatus and diagnostics, present detailed results from one gas puff test, and then present a comparison of two fiber pinch tests, one a "normal" x-pinch and the other a "double-cross."

IV.B Apparatus

A schematic diagram of the experiment for gas puff implosions is shown in Figure IV.1. A puff valve, the design of which was obtained from PI, has an annular nozzle, thereby producing a hollow gas shell with 1.5 cm mean radius, and 0.5 cm thickness. The nozzle mach number is 5 according to an isentropic flow model. The mass load in the gas shell, when optimized to the LION power pulse experimentally, was about $4\mu\text{g}/\text{cm}$ or 10^{17} atoms per cm. This was estimated from the puff pressure measured using a fast ionization gauge. The gas from the supersonic nozzle was preionized by a discharge and imploded by the 30 ns rise time, 550 kA peak current pulse from LION. The gap between the anode and cathode was 1.5 cm and the return current rods were 4.0 cm away from the pinch axis. On some pulses, a plasma opening switch was used to improve the current rise time.

Experimental diagnostics used in the first series of experiments, all of which viewed the plasma from the side, included: a streak camera for time dependent measurements of visible light from the z-pinch or from x-rays impinging upon a scintillator; filtered x-ray diodes and a pin diode to record x-ray and XUV emission in selected spectral regions; a 0.5-m spectrometer to measure visible and UV spectra; and a grazing incidence grating spectrograph to collect soft x-ray spectra. (We are very much indebted to Keith Matzen's group at SNLA for lending us the x-ray spectrograph used for these experiments.) In the second series of experiments, the soft x-ray spectrograph was not available. However, a visible light framing camera was used.

In the gas puff pulses, the amount of implosion mass was "optimized" by adjusting the puff valve plenum pressure such that the pin-diode showed the strongest x-ray emission at or near the pinch time. An early peak on some pin-diode signals resulted from hard x-rays early in the pulse, when the voltage was as high as 800 kV.

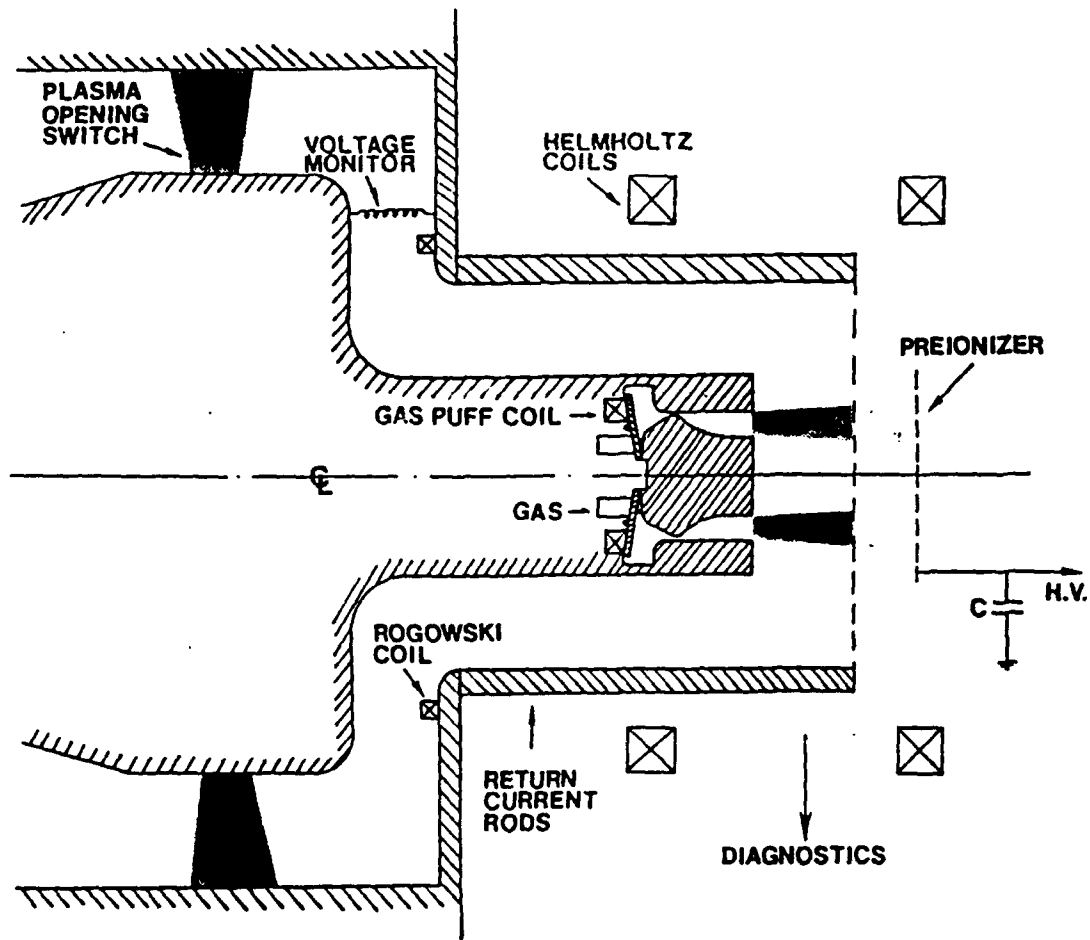


Figure IV.1: Schematic diagram of the z-pinch apparatus when set up for gas puff pulses. There are eight symmetrically placed return current rods and eight side-on diagnostic ports which view between the rods. Preionization of the gas puff in the main z-pinch gap is accomplished by a capacitor discharged through the gas between the downstream diode grid and the preionizer grid.

In order to exemplify the data we obtained, we present details of a gas puff implosion using *CO* gas, after which we will summarize the key features of the ensemble of data obtained in the first set of experiments.

Figure IV.2a shows the current pulse and Fig. IV.2b the voltage pulse for the *CO* shot. The pinch occurred 60 ns after the start of the current as indicated by the changing sign of the voltage. The filtered ($6\mu\text{m}$ mylar) pin-diode signal is shown in Fig. IV.3. Note the half maximum width of 15ns. Figures IV.4a and IV.4b are the soft x-ray emission measured by x-ray (XRDs) diodes with 0.5 and $1.0\mu\text{m}$ aluminum foil filters, respectively. The transmission window of these filters is shown in Fig. IV.5.

The estimated electron density and temperature for the specific *CO* implosion being presented are of the order of $10^{19}/\text{cm}^3$ and 150 eV, respectively. These were obtained using spectroscopy in the following way. Figures IV.6–IV.8 show data obtained with the 0.5m spectrometer at 5292\AA (a CVI line), 2277\AA (a CV line) and 5270\AA (background), respectively. (The first and third wavelength data were obtained on the one shot under discussion here, and the second wavelength data was obtained on another virtually identical pulse.) The first emission peaks shown in Figs. IV.6 and IV.7 correspond to the ionization of carbon ions through four, and then five times ionized at high electron temperature before the pinch is fully formed; the second peak results from recombination after the pinch. For this to occur requires the plasma temperature to be in excess of 60eV.

Strong emission of resonance line radiation from H-like and He-like C and O ions was observed using the soft x-ray spectrometer. Figures IV.9 and IV.10 show portions of time integrated x-ray spectra obtained with a microdensitometer from the x-ray film. Because of the highly uncertain x-ray film (Kodak type 101) calibration, electron temperature information could only be obtained from pairs of lines very close together in wavelength. The line ratio CV 34.97\AA /CVI 33.73\AA yielded

an electron temperature of at least 100eV, and the line ratio of OVIII 18.97Å/OVII 18.63Å yielded at least 140eV. These estimated electron temperatures are lower limits because they correspond to values if the plasma were in equilibrium. Thus, we estimate 150eV.

Electron temperature or density can also be derived from the line ratio of CV 40.73Å/ CV 40.27Å. However, because these are C⁺⁴ lines, the density and temperature are lower than those at pinch time, as strong radiation in these lines occurred before the pinch time.

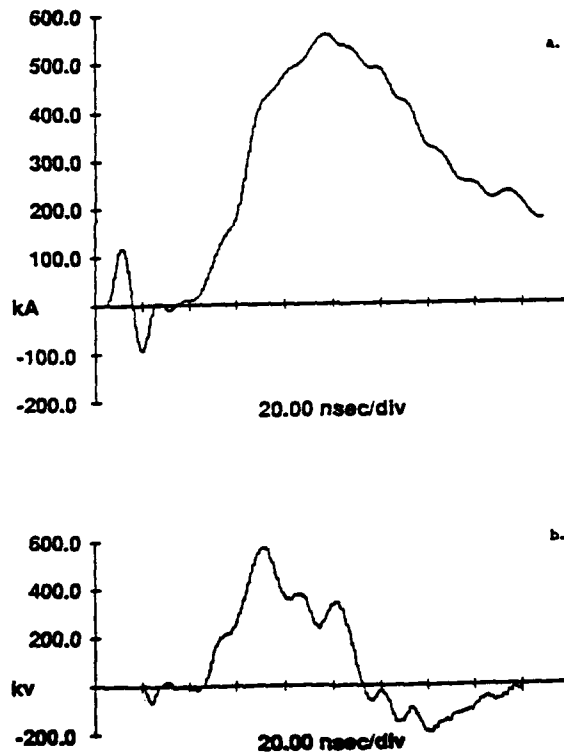


Figure IV.2a: Current (a.) and "corrected" voltage (b.) waveforms for CO gas puff implosion pulse number 313. The negative fiducial mark at the beginning of the voltage waveform corresponds to the time of the negative portion of the fiducial mark on the current waveform.

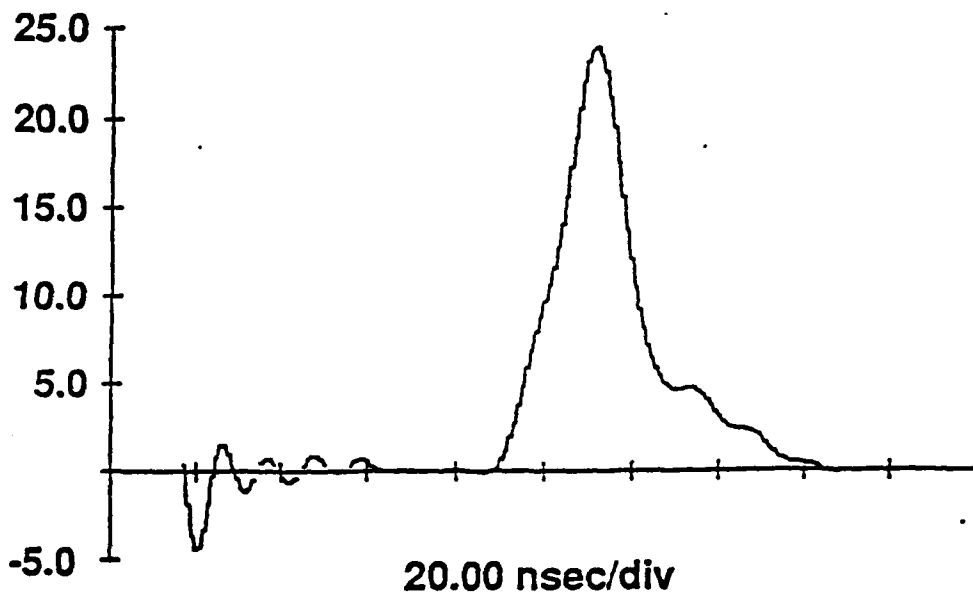


Figure IV.3: Pin diode trace for pulse number 313. A $6\mu\text{m}$ mylar "filter" was used.

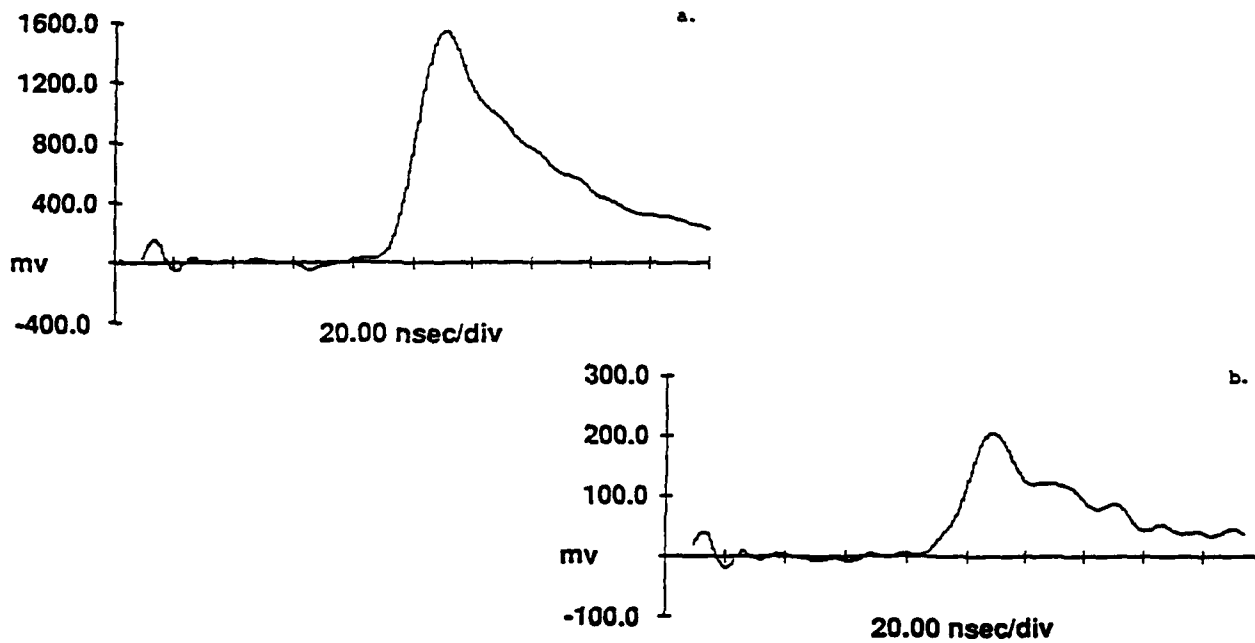


Figure IV.4: XRD signals for shot number 313. The XRD result in (a.) was obtained with a $0.5\mu\text{m}$ aluminum filter while (b.) was obtained with $1.0\mu\text{m}$ of aluminum.

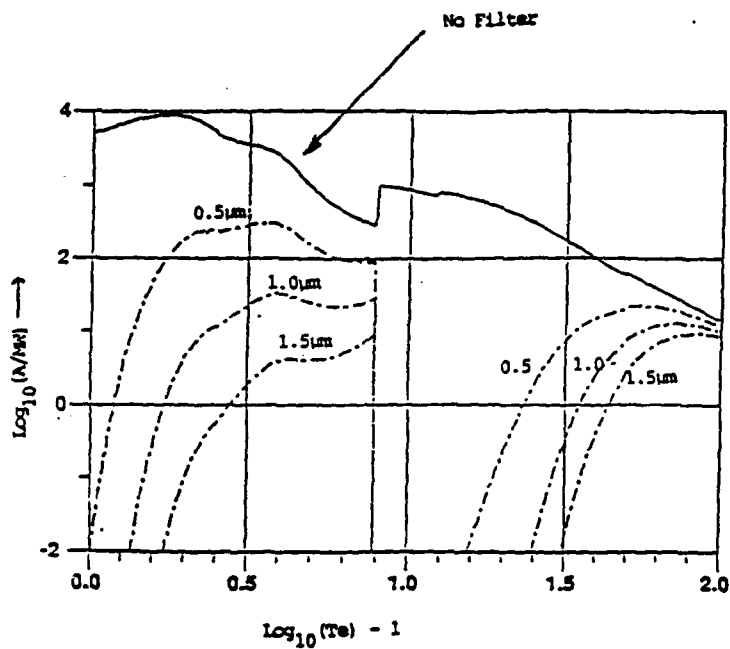


Figure IV.5: XRD response with no filter and with 0.5, 1.0, and 1.5 μm of aluminum foil filters. Notice that the horizontal scale means 1.0 corresponds to 100 eV, etc. In the vertical scale, A/MW \equiv Amperes/Megawatt, is equivalent to 10^{-6} electrons/incident photon.

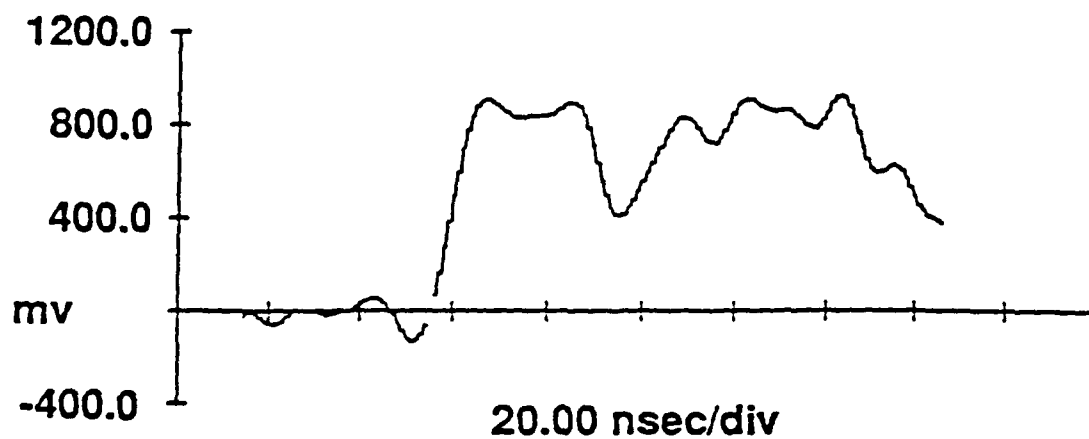


Figure IV.6: Oscillograph of the 5292Å CVI (C^{+5}) line for pulse number 313.

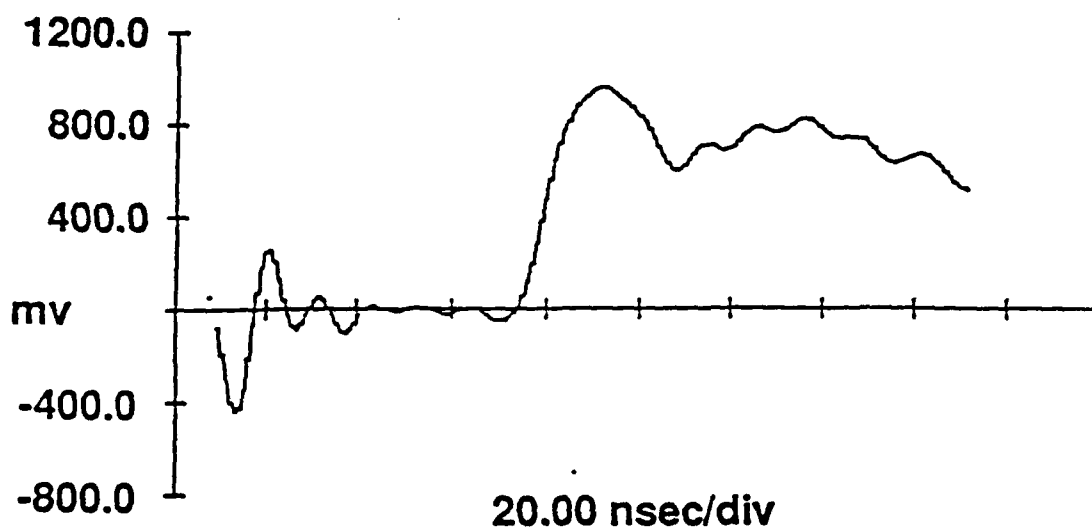


Figure IV.7: Oscilloscope of the 2277Å CV (C^{+4}) line from a shot virtually identical to pulse number 313.

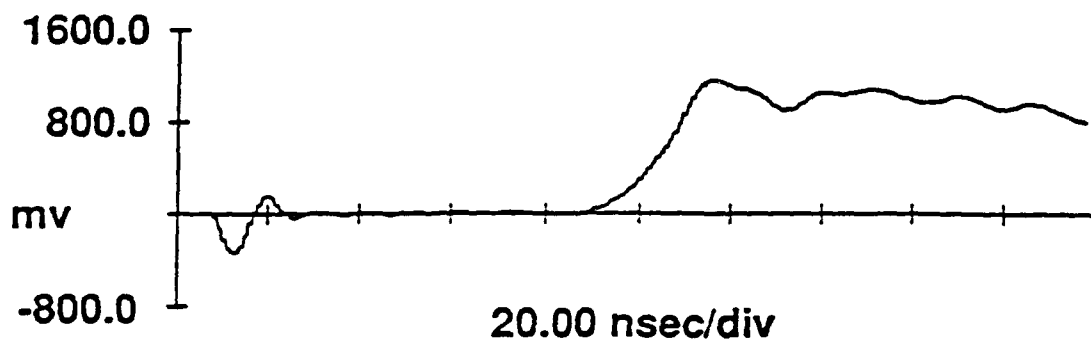


Figure IV.8: Continuum light at 5270Å on pulse number 313. This data was taken together with the 5292Å line radiation shown in Figure 7 by the use of separate fiber optics located at the two spectral positions in the focal plane of the 0.5m spectrometer.

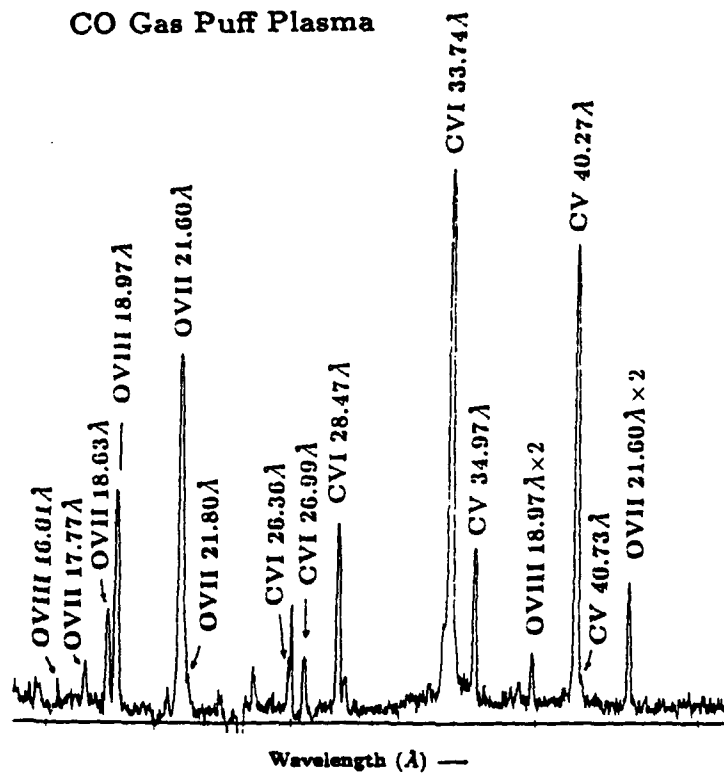


Figure IV.9: Short wavelength data from the x-ray spectrograph from a CO puff pulse.

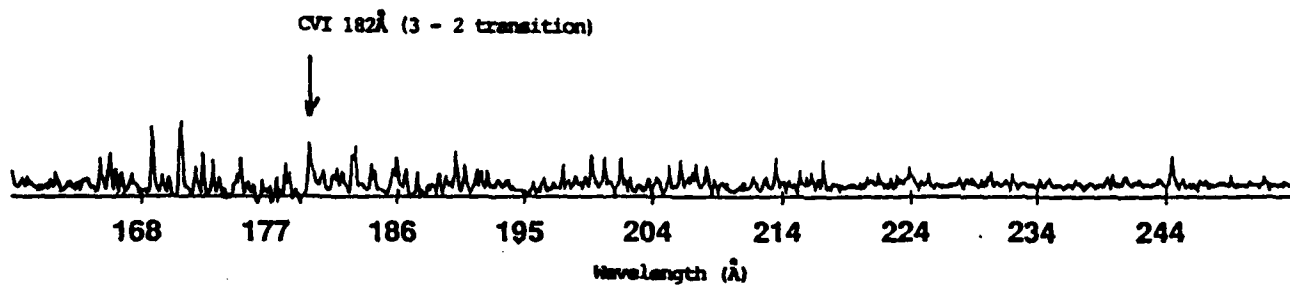


Figure IV.10: Long wavelength data from the x-ray spectrometer for a C_2H_2 puff pulse. Only the 182Å CVI carbon line is indicated although many other peaks in the spectrum are identified as carbon lines. In CO puff pulses, this region of the spectrum contains numerous oxygen lines also.

Knowing the implosion velocity and the time delay between CV line emission and the pinch reaching minimum radius, the estimated pinch density is about 20 times the density from the line ratio technique, namely about $10^{19}/\text{cm}^3$. In fact, using the ratio of intensities of the equivalent *OVII* (O^{+6}) lines, at 21.6Å and 21.8Å, which are radiated much closer to pinch time, we do obtain a density over $10^{19}/\text{cm}^3$. Figure IV.11 shows a streak photograph from a different gas puff pulse. The pinch duration inferred from this photograph is about 10 ns. A 2×10^7 cm/s implosion velocity is also implied by this streak. A pinch radius of 1 mm or less is inferred from streaks using Pilot B scintillator to convert x-rays to visible light which is then viewed by the streak camera.

We now turn briefly to pulses with an applied magnetic field, and then x-pinch loads. When a stabilizing magnetic field of 3 kG was applied using the coils shown in Fig. IV.1, the x-ray intensity on the pin-diode was reduced by a factor of 2.5, and the 33.7Å CVI radiation on the x-ray film was estimated to be a factor of 2 lower. With a magnetic field of 5 kG, the soft x-ray signals were very much weaker.

In the first experimental series, fiber pinch tests utilized only carbon fiber loads. These were configured in the form of an X, touching in the middle. As others have observed before,^{1,2} extremely bright x-ray sources were observed at the fiber crossing point. The point x-ray source (about 1 mm in radius) produced about the same energy in line radiation at CVI 33.7Å as the gas implosion shots. The highest peak emission detected at the pinch time by the x-ray diodes and the pin diode, and the shortest pinch time (less than 5 ns), were obtained with this load configuration. This suggests that the x-pinch plasma is more dense and hotter than the gas puff z-pinch. These results led to the second series of experiments, results from which are described next.

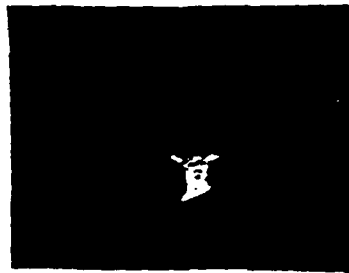


Figure IV.11: Visible light streak photograph of a gas puff implosion using C_2H_2 gas. Time progresses downward. The duration of the "waist" in the streak is 10ns. The width of the waist is 8mm. (The minimum radius observed when x-rays are converted to light with a fast scintillator and then viewed with the streak camera is about 1mm.)

In the second series, normal x-pinchs and "double-cross" fiber pinchs were tested. The gap between the electrodes in which the fibers were mounted was about 4cm. To increase the x-ray radiation yield, combinations of C ($10\mu m$) and Al ($20\mu m$) fibers were used. The estimated soft x-ray radiation yield was several hundred joules, but we do not have detailed spectral information.

Experimental diagnostics included: filtered x-ray diodes (XRDs) to record x-ray emission in selected spectral regions; a visible light framing camera; and a time integrated x-ray pinhole camera. Figures IV.12 and IV.13 show data from single and double-cross (C and Al) fiber shots at the same LION Marx generator charging voltage (80 kV). In these figures, (a) shows the current waveform which peaks at about 500 kA for both cases; (b) shows the inductively corrected load voltage, which is about 900 kV peak, again for both; (c) shows the x-ray radiation ($\gtrsim 1keV$) measured by a pin-diode with a $12\mu m$ Kimfol filter. The x-ray emission is increased by a factor of about 2 for the double-cross pulse; (d) shows the soft x-ray emission ($\gtrsim 500eV$) detected by an XRD with a $1\mu m$ Al foil filter, which increased about 30%; (e) shows the x-ray radiation detected by a scintillator with

$7\mu\text{m}$ Al foil filter and (f) is the monitor of the framing camera with a framing time of 10ns. The initial peak on the pin diode traces in both tests (and perhaps on the XRD traces as well) is believed to be hard (bremsstrahlung) radiation from accelerated electrons when the gap voltage is high. Figures IV.14 and IV.15 show the visible framing and time integrated x-ray images of the single and double-cross fiber shots, respectively, shown in Figs. IV.12 and IV.13. Hot spots at cross points due to harder x-ray emission ($\sim 1\text{keV}$) are clearly visible when a $7\mu\text{m}$ Al filter is used, while the softer x-ray radiation source ($\gtrsim 500\text{eV}$) is imaged when the $1\mu\text{m}$ Al filter is used. The harder x-ray radiation is from a localized region, as shown in Figs. IV.14 and IV.15. The minimum hot spot size indicated by the film is less than $300\mu\text{m}$, which is limited by the $200\mu\text{m}$ pinhole size. These data suggest that most of the harder radiation is from the cross point(s).

IV.C REFERENCES

1. A. A. Kolomensky, A. N. Lebedev, V. A. Papadichev, S. A. Pikus, and B. N. Yablokov, in *Proc. International Conference on High Power Particle Beams*, R. J. Briggs and A. J. Toepfer, Eds., (University of California, San Francisco, 1983), p. 250.
2. Unpublished recent experimental results at Physics International Company and elsewhere have been described to us by Dr. M. Krishnan.

Shot No. zpn462

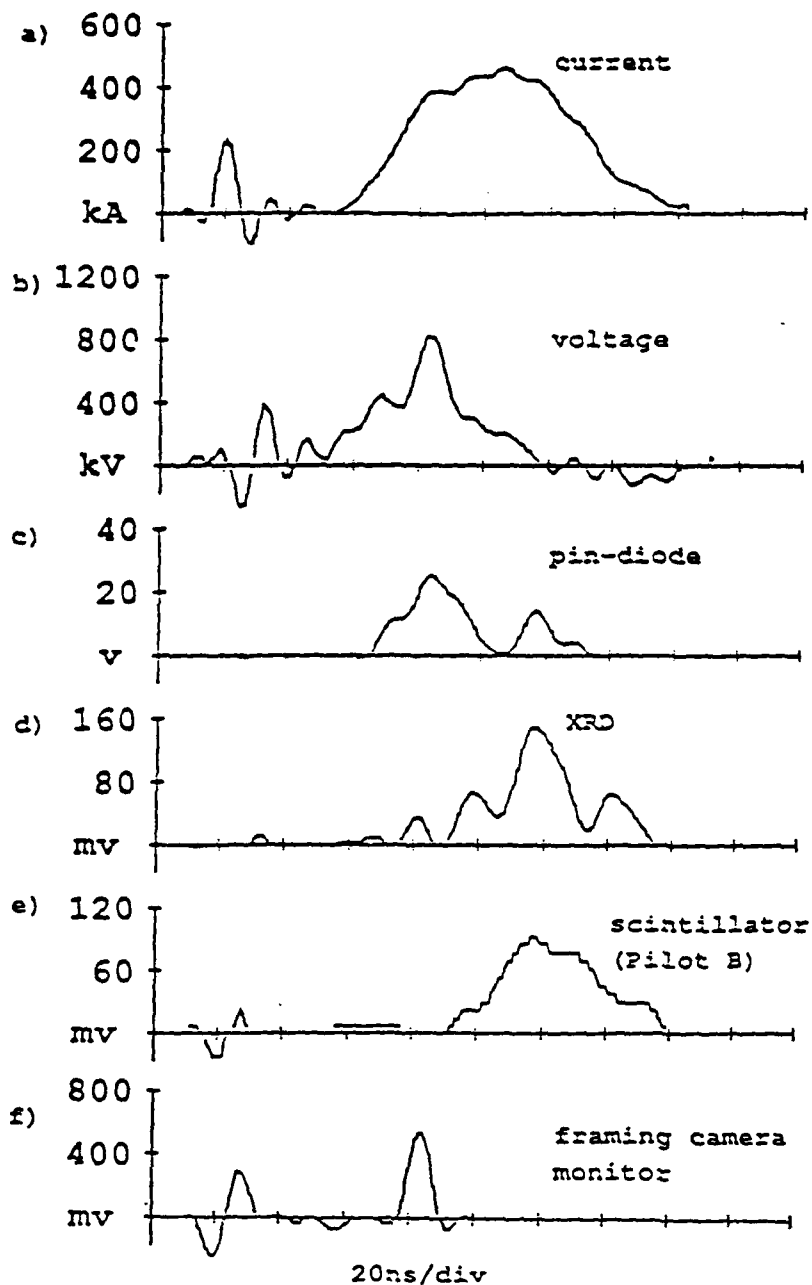


Figure IV.12: Waveforms from an x-pinch pulse showing (a) diode current, (b) load voltage, (c) pin diode with a $12\mu\text{m}$ Kimfol filter, (d) x-ray diode with a $1\mu\text{m}$ aluminum filter, (e) a Pilot B scintillator with a $7\mu\text{m}$ Al filter viewed by a photomultiplier, and (f) visible light framing camera monitor.

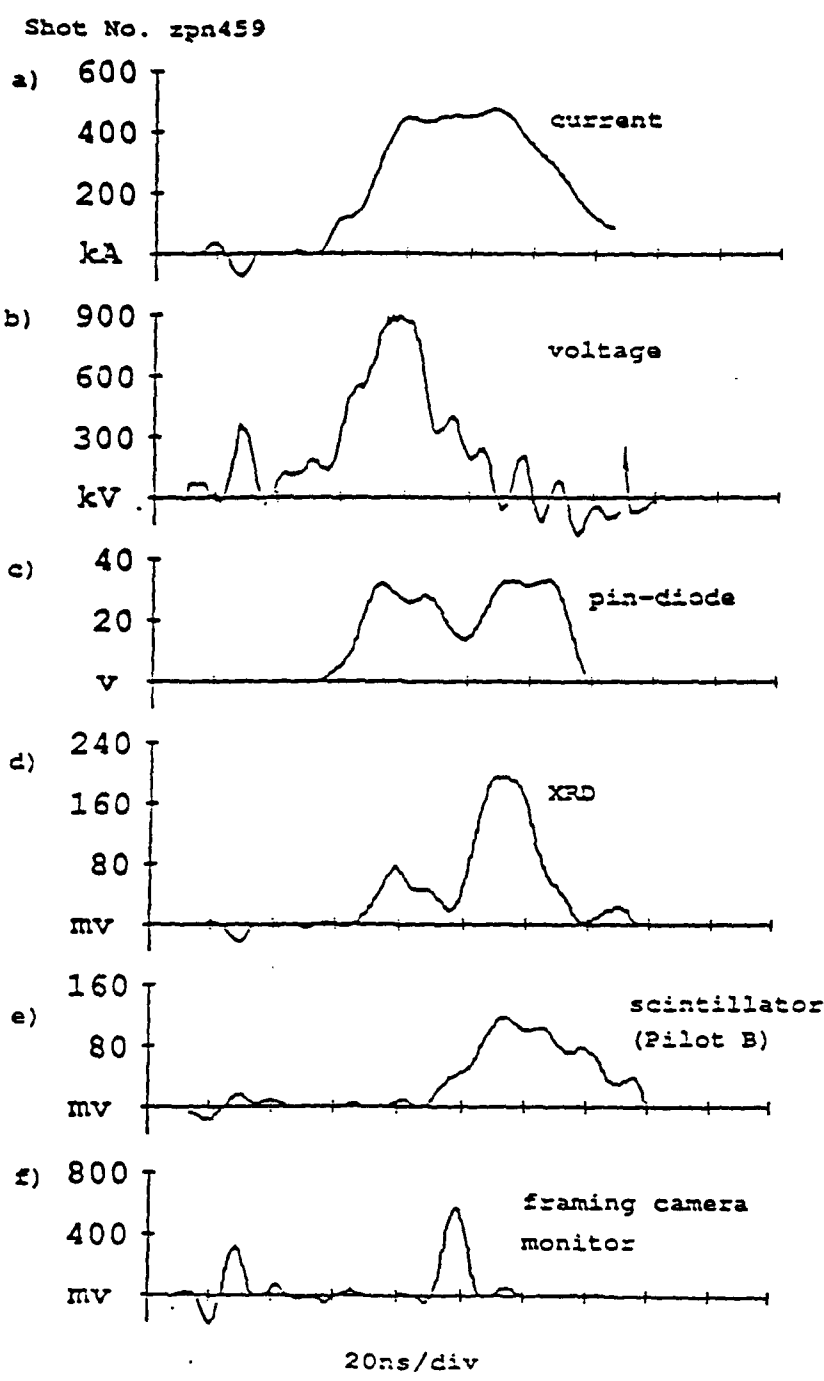
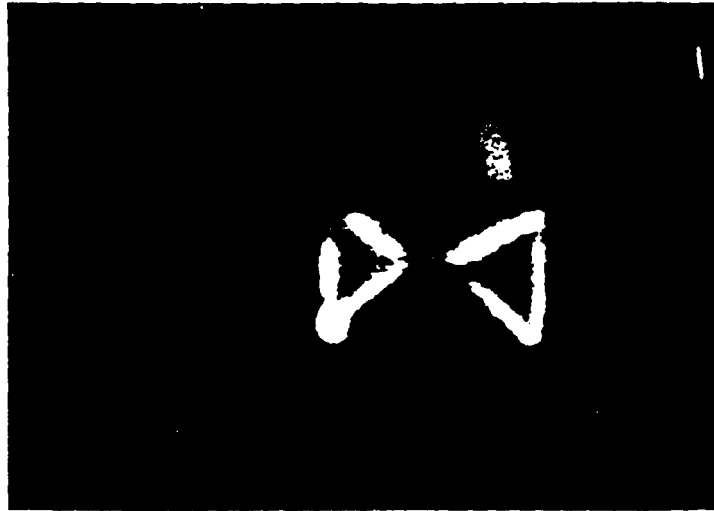
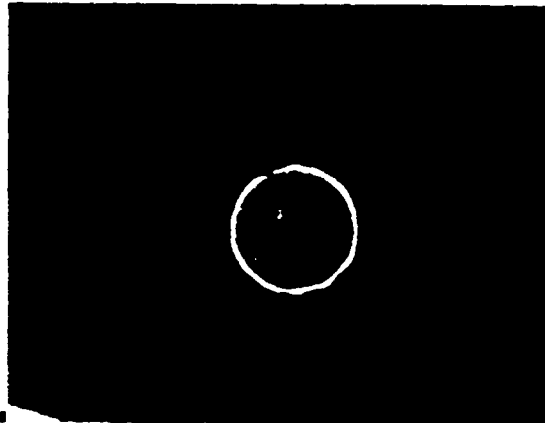


Figure IV.13: Waveforms for a "double-cross" pulse showing (a) diode current, (b) load voltage, (c) pin diode with a $12\mu\text{m}$ Kimfol filter, (d) x-ray diode with a $1\mu\text{m}$ aluminum filter, (e) a Pilot B scintillator with a $7\mu\text{m}$ Al filter viewed by a photomultiplier, and (f) visible light framing camera monitor.

Single Cross Al & C Fibers
Visible framing Camera



X-RAY
0.5mm pin hole;
7 μ m Al foil;
Hotspot size \lesssim 0.5 mm



X-RAY
0.2mm pin hole;
1 μ m Al foil;

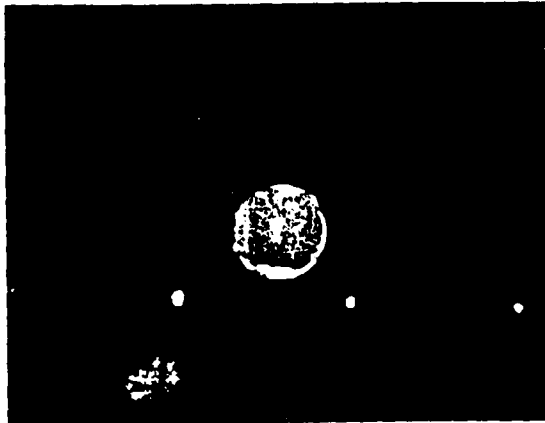
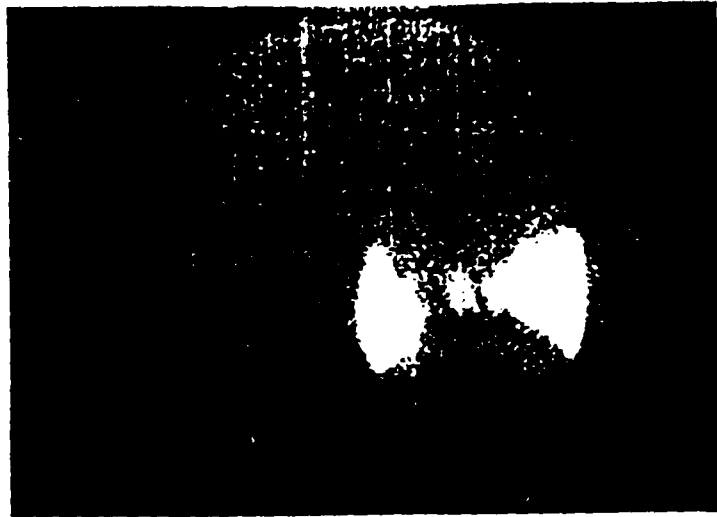
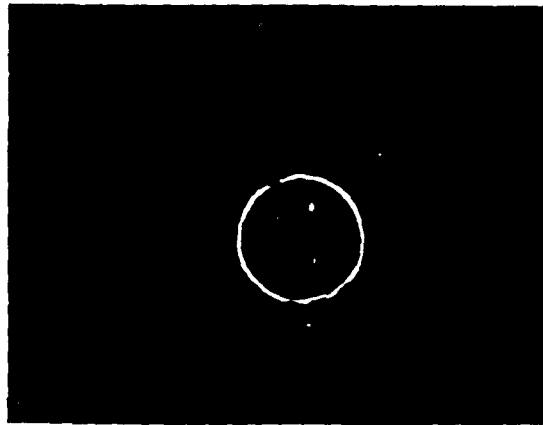


Figure IV.14: Single cross data from the pulse presented in Fig. IV.12, showing a 10ns visible light framing photograph (upper image), a time integrated x-ray pin hole photograph obtained with a 7 μ m Al foil filter and a time integrated x-ray pin hole photograph obtained with a 1 μ m Al foil filter.

Double Cross Al & C Fibers
Visible Framing Camera



X-RAY
0.5mm pin hole;
7 μ m Al foil;
Two hot spots are
10mm apart



X-RAY
0.2mm pin hole;
1 μ m Al foil;
Hot spot size \lesssim 300 μ m



Figure IV.15: Double cross data from the pulse presented in Fig. IV.13 showing a 10ns visible light framing photograph (upper image), a time integrated x-ray pin hole photograph obtained with a 7 μ m Al foil filter and a time integrated x-ray pin hole photograph obtained with a 1 μ m Al foil filter. For scale, the two hot spots in the middle and lower photographs are 10mm apart.